



Microstructural Evolution and Mechanical Properties of Multiwall Carbon Nanotubes Reinforced Titanium-Based Nanocomposites Developed by Spark Plasma Sintering

Avwersuoghene Moses Okoro¹ · Ronald Machaka² · Senzeni Siphon Lephuthing¹ · Mary Ajimegoh Awotunde¹ · Peter Apata Olubambi¹

Received: 5 April 2020 / Accepted: 19 May 2020 / Published online: 22 June 2020
© The Korean Institute of Metals and Materials 2020

Abstract

In this study, the role of multiwall carbon nanotubes (MWCNT) on the microstructural evolution and mechanical properties of Ti6Al4V-based composites was investigated. This was conducted by dispersing different concentrations (0.5, 1.0 and 1.5 wt%) of MWCNT into the Ti6Al4V matrix using shift-speed ball milling technique. Thereafter, the Ti6Al4V and the nanocomposites were consolidated via the spark plasma sintering technique. Various characterization techniques; scanning electron microscopy (SEM), transmission electron microscopy (TEM) and light microscopy were conducted to understand the microstructural evolution of the samples after the dispersion and sintering process. Subsequently, micromechanical and nanoindentation was carried out to reveal the mechanical properties of the fabricated samples. The morphological examination using SEM and TEM revealed the dispersibility of MWCNT dispersed within the Ti6Al4V matrix. Besides, the selected area diffraction and the fast Fourier Transform pattern demonstrated that the increase in concentration of the MWCNT exposed the nanotubes to adverse stresses during the dispersion process. Furthermore, the incorporation and increase in concentration of the MWCNT in the titanium alloy resulted in microstructural and phase changes, which translate to tremendous improvements in microhardness, nanohardness and elastic modulus up to 46.9%, 150.8%, and 169.5% respectively.

Keywords Microstructural evolution · Mechanical properties · Titanium alloy · Multiwall carbon nanotubes · Spark plasma sintering

1 Introduction

Multiwall carbon nanotubes (MWCNT) are highly desirable in diverse engineering applications due to their notable thermal, mechanical and electrical properties [1]. They have tubular morphology with ultra-high aspect ratio in the range of 100–100,000 and lightweight of 1.7–2.0 g/cm³ [2]. Additionally, it has a tensile strength close to 150 GPa, a distinctly high elastic modulus of up to 1TP [3], thermal

conductivity of up to 0.000004 W/m/K [4] and electrical conductivity of 0.000002 Ωcm [5]. These outstanding properties of MWCNT are traceable to the strong graphitic carbon to carbon network in its structures, nanoscale dimensions and tubular morphology [6–8]. MWCNT has been successfully utilized as a reinforcing material to improve the thermal, mechanical and electrical properties of various engineering materials. In recent years, properties such as toughness of ceramics has been effectively enhanced using MWCNT [9] and strength of polymeric materials has been augmented by MWCNT [10]. It has been used to improve the lightweight, strength, toughness and tribological properties of various metal matrices to form metal matrix composites [11–13].

Amongst the metal matrix composites used in numerous engineering applications, the demand for titanium-based nanocomposites have spurred unprecedented attention in various automobile, biomedical and aerospace industries [14]. Furthermore, titanium and its alloys are highly

✉ Avwersuoghene Moses Okoro
okoromo@gmail.com

¹ Centre for Nanoengineering and Tribocorrosion, Department of Metallurgy, School of Mining, Metallurgy and Chemical Engineering, University of Johannesburg, Doornfontein Campus, Johannesburg 2028, Republic of South Africa

² Titanium Centre of Competence, Council for Scientific and Industrial Research, P.O. Box 395, Pretoria 0001, South Africa

desirable in various industrial and technological applications owing to their excellent corrosion resistance, biocompatibility, weldability, specific strength and lightweight [15–17]. Titanium alloys are classified into various grades depending on their compositions, phases and properties. However, the grade 5 of the titanium alloy popularly called Ti6Al4V is the most highly employed titanium alloy for various applications owing to its higher strength and heat-treatability [18]. It has a dual phase microstructure consisting of the alpha and beta phases, which changes at various operating temperatures. The alpha phases exist at lower operating temperatures below 884 °C and it has a hexagonal closed packed structure (HCP). Conversely, the beta phase occurs at higher operating temperatures (between 884–1668 °C) with body centered cubic structure (BCC) [19]. The combination of the different crystal structures resulting from allotropic transformation in the dual phase titanium alloy is responsible for its improved properties than other grades of titanium-based alloy.

Regardless of the outstanding properties and flexibility of Ti6Al4V, its elastic modulus is twice as less as the elastic modulus of iron [20]. This implies that the elastic strain energy required for the formation of a new phase in Ti6Al4V during allotropic transformation is lesser than elastic strain energy during the allotropic transformation of iron. Additionally, it possessed low wear resistance and hardness that is far lesser than that of super-duplex stainless steels and nickel-based alloys, which are widely applied in the production of turbine blades [21].

In recent years, various attempts have been made to augment the mechanical properties of Ti6Al4V using numerous ceramics-based reinforcements by fabricating titanium matrix composites. Falodun et al. [22] achieved tremendous improvement in the hardness Ti6Al4V after reinforcing the alloy with TiN and TiCN. Similarly, Zhao et al. [23] reported an improvement in the tribological properties of Ti6Al4V reinforced with titanium carbide (TiC) and titanium diboride (TiB) powders. However, owing to the remarkable properties of MWCNT has shown that it's a best candidate to augment the properties of Ti6Al4V.

Past studies have shown the effectiveness of MWCNT in improving the mechanical properties of various titanium-based materials. This was reported by Kondoh et al. [24], whose work confirmed the improvement in tensile strength, yield strength, microhardness and strain of commercially pure titanium by the incorporation of MWCNT as reinforcement phase. Similarly, Sun et al. [25] recorded an improvement in ultimate tensile strength and hardness of titanium by reinforcing it with MWCNT. Additionally, Munir et al. [13] realized an improvement in the mechanical and tribological properties of titanium by the integration of MWCNT into its matrix. These improvements in properties of titanium are traceable to the uniform dispersion, load-carrying abilities and unique mechanical properties of MWCNT.

To fabricate titanium-based nanocomposites using MWCNT as reinforcing materials, it is pertinent to accomplish uniform dispersion of MWCNT in the titanium-based matrices without compromising its structural integrity. This is paramount for effective load transfer from the matrix to the reinforcement phase. However, MWCNT tend to cluster into bundles which inhibits their homogeneous dispersion in the metal matrix [8, 26]. The clustering of MWCNT is usually ascribed to the strong Van der Waal forces between its tubes, nanoscale dimensions and high aspect ratio [27]. Conversely, an effective dispersion technique is required to achieve uniform dispersion of MWCNT in metal matrices without destroying the structures of the MWCNT. High energy ball mill has been widely employed to disperse MWCNT, but it leads to the damages of the nanotubes structure especially when regulated milling parameters are not used. The destruction of the walls of the MWCNT results in the conversion of the sp^2 carbon to carbon network into sp^3 (amorphous carbon), which can easily react with the titanium to form interfacial products (carbides) [28]. Meanwhile, the interfacial products can assist in load bearing capability of the composites alongside with the reinforcing ability of the MWCNT, thus resulting in a composites with improved mechanical properties [29]. Besides the utilization of MWCNT to enhance the properties of titanium-based matrices, the application of improved consolidation technique is very paramount in synthesizing nanocomposites with enhanced properties.

Over the years, spark plasma sintering (SPS) which is an improved consolidation technique has been successfully utilized to fabricate titanium-based nanocomposites of outstanding properties. This was reported by Munir et al. [1], where improvement in elastic modulus and nanohardness was achieved on commercially pure titanium using MWCNT as reinforcement and SPS as the consolidation technique. Likewise, Wang et al. [30], achieved a tremendous improvement in compressive strength of up to 61% on pure titanium after reinforcing the metal matrix with MWCNT and sintering the compact with SPS technique. Additionally, they reported an improvement in the microhardness and thermal diffusivity of the fabricated composites with the incorporation and increase in concentration of MWCNT. These improvements in mechanical and tribological properties of pure titanium by the incorporation of MWCNT can be ascribed to the load-bearing ability of the MWCNT and the modification of the microstructure titanium matrix. Owing to the interfacial reaction between MWCNT and the titanium matrix during milling or sintering, a hard carbide phase (TiC) is usually formed which assist in augmenting the mechanical and tribological properties of the titanium during the incorporation of MWCNT [31]. In incorporation, the strengthening of the titanium matrix may be linked to the dispersion of the MWCNT in the metal matrix, which

in turn helps to pin down dislocation motion during plastic deformation of the composites [32].

To date, the influence of MWCNT incorporation on the microstructural evolution, mechanical properties and fracture behaviour of Ti6Al4V has not been satisfactorily studied yet. Hence, in this study, MWCNT of varying concentrations were dispersed in Ti6Al4V using shift speed ball milling. Afterwards, the admixed powders were sintered using the SPS technique. Furthermore, the microstructural changes, mechanical and fracture behaviour of the sintered nanocomposites were quantitatively investigated.

2 Experimental

2.1 As-Received Materials

The NX7100- A -Ultra purified MWCNT used for this study has 99.7% purity and it was acquired from Nanocyl Belgium. It has an inner and outer diameter of 7–8 nm and 9–10 nm respectively. While, the matrix material is a prealloyed Ti6Al4V powders with average particle size of 25 μm and was purchased from TLS Technik GmbH & Co Germany. The stearic acid used as a process control agent during the milling of the powders was procured from Glass blown & Volumetric Glassware & Chemicals in Johannesburg, South Africa.

2.2 Dispersion of MWCNT in Ti6Al4V Matrix

The Ti6Al4V powders was weighed alongside with MWCNT powders of varying concentrations (0.5, 1.0 & 1.5 wt%) and stearic acid (1.0 wt%) and charged into a steel vial. The steel vial consists of outer diameter of 250 mm and inner diameter of 100 mm. Steel balls of 5 mm and 10 mm were added to the measured powders as milling aid. The milling operation was then conducted using shift speed ball milling technique (SSBM), which was carried out by transferring the measured powders into a low-speed ball mill (Retch 100 PM) for preliminary milling operation. This milling operation was carried out using the following milling parameters; milling speed of 150 revolution per minute (rpm), time of 8 h and ball to powders weight ratio (BPWR) of 10:1 respectively. Meanwhile, a relaxation time of 10 min for every 10 min of milling was used to prevent the charged powders from overheating and to minimize the tendency of interfacial reaction during the milling operation.

Afterwards, the steel vial comprising the milled powders was transferred into a high-speed ball mill (Retch 400 PM) for subsequent milling to aid homogeneous dispersion of the MWCNT in the Ti6Al4V powders. The subsequent milling operation was carried out with a speed of 100 rpm for 1 h using the same BPWR as the preliminary milling operation.

2.3 Sintering of the Ti6Al4V and Ti6Al4V Nanocomposites Reinforced with MWCNT

Prior to the sintering operation, the admixed powders were weighed and charged into a cylindrical graphite die of \varnothing 20 mm diameter. Subsequently, the charged powders were compacted under a force of 10 KN to promote green strength and conductivity between the die and the charged powders. Afterwards, the compacted nanocomposite powder was transferred into the SPS (model HHPD-25, FCT Systeme Germany) sintering chamber for the fabrication process. The sintering parameters used for the fabrication process include sintering temperature of 1000 $^{\circ}\text{C}$, heating rate of 100 $^{\circ}\text{C}/\text{min}$, compacting pressure of 50 MPa, and holding time of 10 min. After the fabrication process, the sintered samples were left to cool in the sintering chamber and subsequently sandblasted to remove graphite foils from the surface.

2.4 Characterization of Powders and Fabricated Nanocomposites

To understand the morphology of the as-received and the mixed powders after the SSBM operations, the microstructural features of the powders were characterized using scanning electron microscope (Carl Zeiss Sigma FESEM) and JEOL-Jem 2100 transmission electron microscope (TEM). TEM was used to evaluate the walls of the MWCNT to reveal the structure of the nanotubes before and after dispersion in the Ti6Al4V matrix. Also, TEM was used to capture the fast Fourier transform (FFT) of the powders. This is to evaluate the interlayer spacing and the crystalline nature of the nanotubes before and after dispersion. The phase analysis of the powders and sintered nanocomposites were characterized using X-Ray diffractometer (XRD, Rigaku D/max-rB) to assess the changes in the phases of the powders during SSBM and sintering operation. The analysis was investigated by scanning the materials using Cu-K α ($\lambda = 0.154$ nm) radiation over an angular range of 10 $^{\circ}$ –90 $^{\circ}$ at a scanning rate of 1 $^{\circ}/\text{min}$. The various phases present in the material were assessed using ICDD card reference data.

The structural integrity of the acquired MWCNT and MWCNT in the Ti6Al4V matrix after dispersion, and sintering operation was investigated using Raman spectroscopy (WITEC 2.10). This was carried out by acquiring the Raman spectra of the powders and the sintered nanocomposites in the range of 200 to 1800 cm^{-1} after probing ten various spots on the materials using a 514 nm laser beam at an acquisition of 50 s. Furthermore, the intensity of the acquired Raman peaks (D-band and G-band) and their corresponding positions on the Raman shift were assessed by deconvoluting the Raman spectra using the WITEC 2.10 software. Meanwhile, the Raman shifts were calibrated in accordance to ASTM E1840-96 [33].

Subsequently, the metallographic preparation (grinding) was done on the sintered samples using silicon carbide papers with various grit sizes (P320–1200). Afterwards, the samples were further grind using Aker Allegra 3 plate with 6 μm suspension to remove induced scratches from the samples. Finally, polishing was carried out using fused silica suspension to obtain the mirror-like feature of the samples. The polished samples were later characterized using light microscope (LM) and SEM. Also, the fractured surface of the samples was analyzed using SEM.

2.5 Density Measurement and Mechanical Test of the Fabricated Materials

The theoretical density of the fabricated Ti6Al4V and the Ti6Al4V based nanocomposites was calculated by the application of the composite rule of mixture bearing in mind that the theoretical densities of Ti6Al4V and MWCNT are 4.43 g/cm^3 and 2.11 g/cm^3 respectively. While the experimental density was ascertained from the arithmetic mean of five different density readings for each sample in accordance to ASTM B962 using the Archimedes' principle [34]. Furthermore, the densification was calculated by dividing the average density reading by the theoretical density and multiplying the result by 100%.

Subsequently, the Vickers microhardness values of the sintered alloy and the nanocomposites were investigated using INNOVA FALCON 500 series microhardness tester. This was carried out by indenting the polished surface of the sample using a diamond indenter and load of 100 gf (0.98 N) at a dwelling time of 10 s. Various phases of the sample were indented and the mean value was reported for the Vickers hardness value of the material. Furthermore, nanoindentation was carried out on the polished samples using ultra nanoindenter (UNHT) with a load of 100 mN. An average of 15 indentations were made on the polished sample to ascertain the reliability of the data generated. The major mechanical properties determined from the nanoindentation study were reduced elastic modulus and hardness, which were evaluated from the load–displacement data in accordance with Oliver and Pharr method [35]. The reduced elastic modulus (E_r) was calculated from the unloading part of the load–displacement curve. Meanwhile, the nanohardness was calculated by the application of the expression in Eq. (1), which indicates that nanohardness (H_N) has a relationship with the maximum load (P_{max}) and the projected contact area (A_c) at the maximum load.

$$H_N = \frac{P_{max}}{A_c} \quad (1)$$

Besides, the reduced elastic modulus can be calculated from Eq. (2), where E_s and E_i are the elastic modulus of the sample and the indenter respectively [36].

$$\frac{1}{E_r} = \frac{1 - \nu_s^2}{E_s} + \frac{1 - \nu_i^2}{E_i} \quad (2)$$

3 Results and Discussion

3.1 Microstructural Analysis

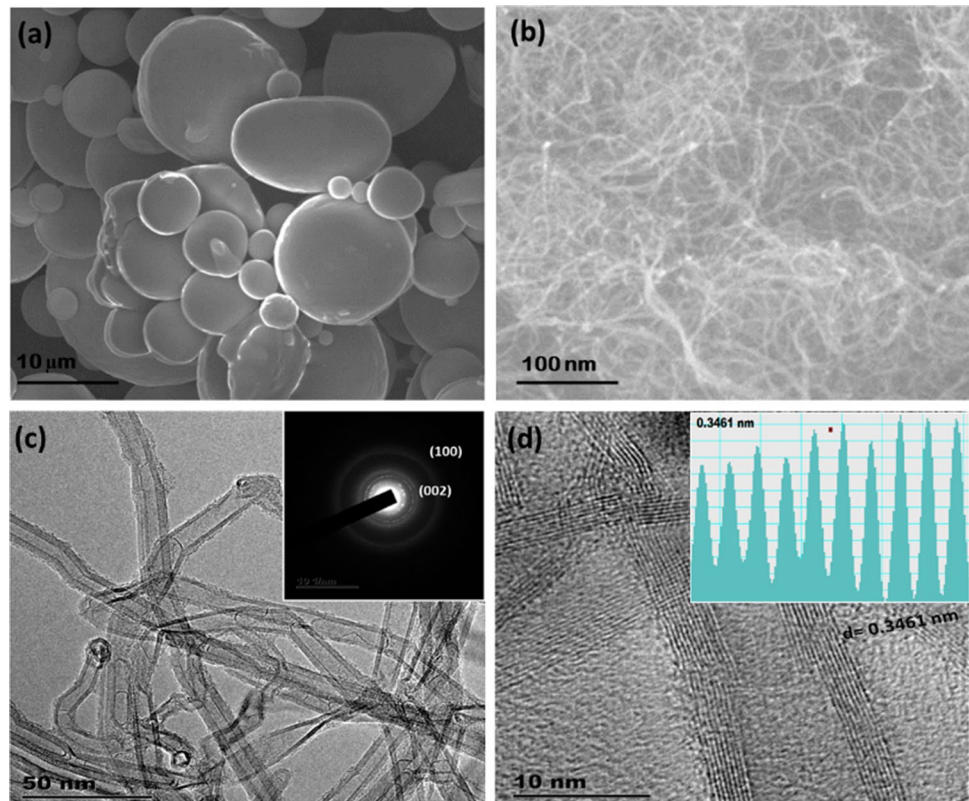
The microstructural analysis of the starting powders was carried out using SEM and TEM to ascertain the morphological features prior to the dispersion process. This is shown in Fig. 1a–d. The SEM micrograph in Fig. 1a represents the spherical features of the Ti6Al4V particles with average size of 25 μm while Fig. 1b shows the SEM micrograph of the as-received MWCNT, which depicts the clustering of the individual multiwall nanotubes.

Moreover, the TEM micrograph in Fig. 1c revealed the tubular morphology of the clustered pristine MWCNT while the inset shows the selected area diffraction pattern (SAED) of the as-received nanotubes. The SAED pattern is usually employed to confirm the amorphous and crystalline phases of the MWCNT before and after their dispersion in the matrix materials. The SAED pattern in Fig. 1c shows the clear rings of the graphitic planes (002) and (100) which depicts the crystalline nature of the nanotubes without any alterations of the planes [37]. Besides, a highly crystalline nanotubes is associated with similar chirality and sharp coaxial rings with fewer halo ring pattern [8]. Furthermore, the TEM micrograph in Fig. 1d shows the walls of the tubular structure of the MWCNT while the inset depicts the fast Fourier transform (FFT) pattern of the pristine nanotubes. From Fig. 1d, it was observed that there was no trace of defects in the form of deformation on the walls of the nanotubes with interlayer spacing of 0.3461 nm. This was further confirmed by the FFT pattern which shows sharp narrow peaks which indicates high crystalline nature of the pristine MWCNT [38].

3.1.1 Effect of SSBM on the Dispersibility of MWCNT in Ti6Al4V Powders

Over the years, emphasis has been made on the effective transfer of the unique properties of MWCNT into matrix materials during composite production. To realize the transfer of the nanotubes' properties into the matrix materials, the uniform dispersion and interfacial bonding of the MWCNT in the matrix must be accomplished without conceding the tubular structures of the nanotubes during dispersion [1]. Additionally, to realize homogenous dispersion and good interfacial bonding during the dispersion process requires adequate impact energy to curb the strong Van der Waals

Fig. 1 SEM micrographs of the starting Ti6Al4V **a**, MWCNT **b**, and TEM micrograph of MWCNT **c** alongside the FFT (inset) of the powders



forces that occurs between the individual nanotubes [39]. The essence of the adequate impact energy during dispersion is to induce forces to de-entangle the clustered MWCNT and spread it across the matrix materials. However, the impact energy should not be too high, such that it introduces structural defects on the walls of the nanotubes.

Although, numerous techniques have been employed in recent years to achieve the uniform dispersion of MWCNT in various metal matrices [6, 40, 41]. However, this study employs the use of shift speed ball milling technique to uniformly disperse MWCNT into Ti6Al4V matrix. This technique involves the application of both low-speed ball mill and high-speed ball mill with regulated milling parameters to foster the homogenous dispersion of MWCNT [8, 42]. The SEM micrographs in Fig. 2 (a-c) shows the dispersion features of MWCNT in Ti6Al4V powders after SSBM.

From the SEM micrograph in Fig. 2a, which shows the dispersion features of the mixed powder comprising of 0.5 wt% MWCNT, it was observed that there was homogenous dispersion of the nanotubes within the Ti6Al4V matrix. In addition, good adhesion between the nanotubes and the Ti6Al4V particles was noticed. This was confirmed from the inset in Fig. 2a, which shows the microstructural evolution and bonding at higher magnification. The microstructural evolution, good adhesion and dispersion characteristics of the MWCNT in the mixed powder of this nanocomposite grade is ascribed to the adequate impact energy exerted on

the powders during SSBM that resulted in the deagglomeration and uniform dispersion of the nanotubes in the Ti6Al4V matrix.

The SEM micrograph in Fig. 2b shows the microstructural evolution, dispersion features and bonding of the 1.0 wt% MWCNT in Ti6Al4V powders. From the SEM micrograph, homogenous dispersion and good bonding of the nanotubes to the Ti6Al4V particles was observed. Furthermore, the inset in the SEM micrograph also depicts the embedment of the nanotubes in the Ti6Al4V particles which represents good bonding between the composite components. The good adhesion and dispersion features of the MWCNT achieved during SSBM can be ascribed to the sufficient impact energy exerted on the powders during the dispersion process. Moreover, the SEM micrograph in Fig. 2c shows the dispersion features of 1.5 wt% MWCNT in the Ti6Al4V powders. From the SEM micrograph, MWCNT were agglomerated at various interstitial sites of the Ti6Al4V particles, which indicates that the nanotubes were not fully dispersed in the matrix materials. The inset in Fig. 2c further confirmed the agglomeration of the nanotubes on the Ti6Al4V matrix. From the dispersion features of the nanotubes, it can be deduced that there are stronger Van der Waal forces with increase in the concentration of MWCNT in this composite grade. Therefore, to achieve adequate dispersion of the 1.5 wt% MWCNT in the Ti6Al4V powders, it is pertinent to increase the milling parameters so as produce an adequate

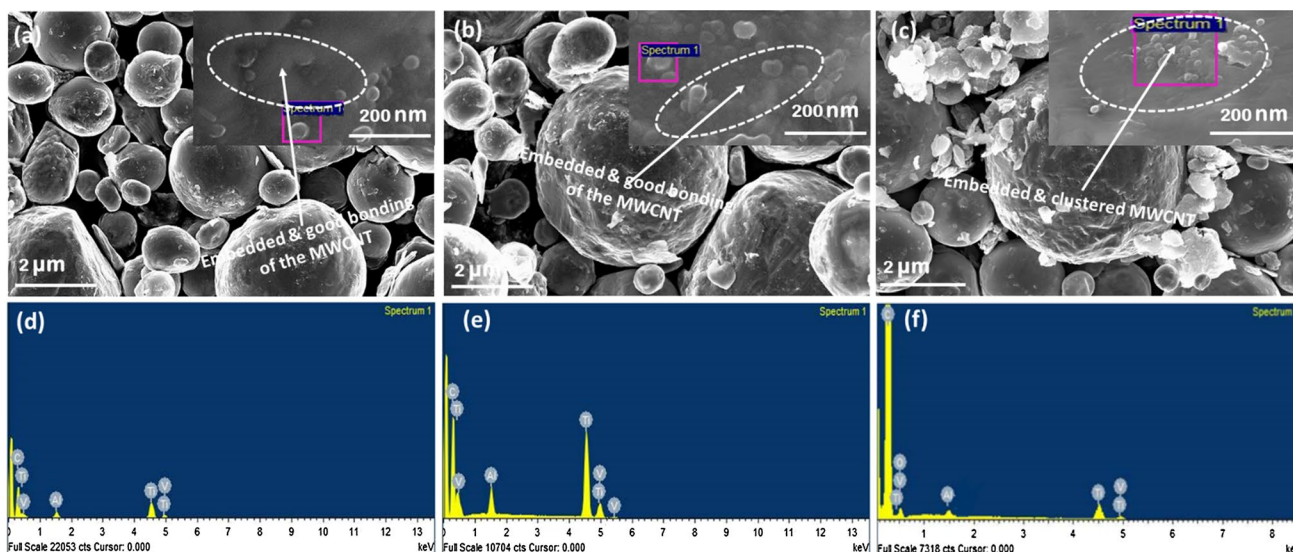


Fig. 2 SEM micrographs of the mixed composite powders (MWCNT-Ti6Al4V) comprising of 0.5 wt% **a**, 1.0 wt% **b** and 1.5 wt% MWCNT **c** and their conforming EDX **d–f**

impact energy that will eventually curb the stronger Van der Waal forces and de-entangle the nanotubes.

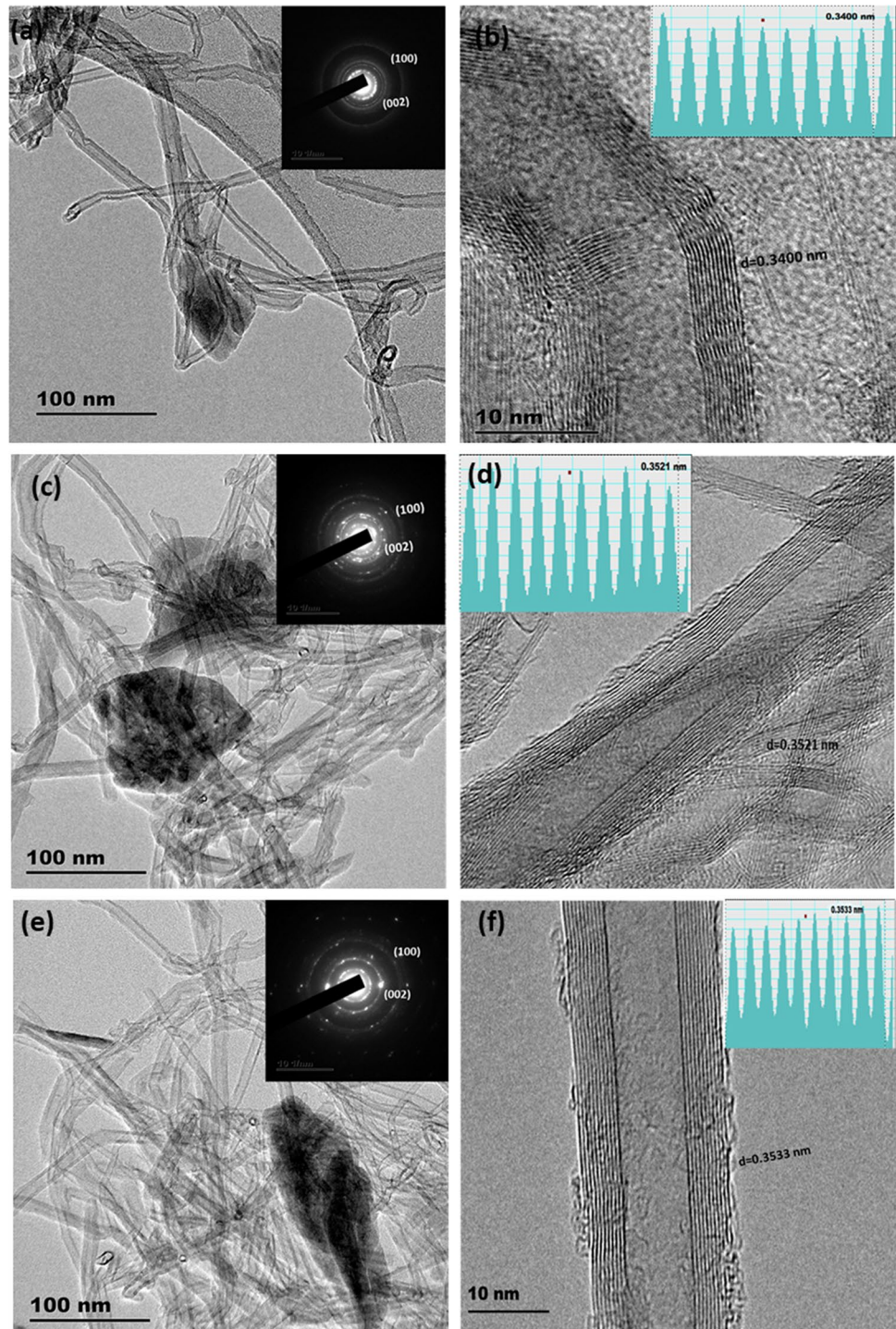
To further ascertain the nanostructural evolution, dispersive features and the structural integrity of MWCNT, the mixed powders were characterized using high-resolution transmission electron microscope (HRTEM). The results of the HRTEM analysis are shown in Fig. 3a–f. Figure 3a, which presents the morphology of the mixed powders comprising of 0.5 wt% MWCNT, indicates the de-entangled, embedded and dispersed nanotubes around the Ti6Al4V powder. Meanwhile, the inset in Fig. 3a shows the SAED pattern of the nanotubes after dispersion in the metal matrix. From the SAED pattern, sharp rings of the graphite planes were observed, which depicts the crystalline nature of the nanotubes after the dispersion process. However, some distortion were observed in the walls of the MWCNT, which is shown in the TEM micrograph in Fig. 3b. As shown in the inset in the TEM micrograph, which represents the FFT pattern of the MWCNT after the dispersion process, a reduction in the interlayer spacing from 0.3461 nm in the pristine MWCNT to 0.3400 nm was observed. The reduction and distortion in the walls of the nanotubes may be ascribed the collapse of the walls during the dispersion process. However, the collapse of the walls of nanotubes cannot be attributed to severe defects (open edges and vacancies), which may have appeared in the form of streaks and extra spots on the SAED pattern in Fig. 3a [43].

The TEM micrograph in Fig. 3c represents the morphology of the mixed powders comprising of 1.0 wt% MWCNT. From the TEM micrograph, the dispersed, deagglomerated and embedded nanotubes were observed after the SSBM process. Moreover, the inset in Fig. 3c shows the SAED

pattern of the MWCNT after the dispersion process which depicts the fading out of the coaxial and halo ring patterns. This feature may be attributed to the strain exerted on the MWCNT during the dispersion process. This is because an increase in the concentration of the nanotubes in the composite grade exposed more MWCNT to collision with the balls during milling. The TEM micrograph in Fig. 3d shows the walls of the MWCNT while the inset indicates the FFT pattern of the nanotubes after the SSBM process. From the TEM and the FFT pattern in Fig. 3d, distortions were observed in the walls of the nanotubes during the dispersion process. This resulted in an increase of the interlayer spacing of the walls from 0.3461 nm in the pristine MWCNT to 0.3521 nm after dispersion. The increase in the interlayer spacing and the fading out of the coaxial and halo rings of the nanotubes may be ascribed to the adequate collision of the balls on the MWCNT, which exerted some stresses on the powders during the dispersion.

Furthermore, the TEM result in Fig. 3e shows the dispersion features of the 1.5 wt% MWCNT in the Ti6Al4V powders. From the TEM micrograph, it was observed that more nanotubes were segregated out from the Ti6Al4V powders, which is an indication of stronger Van der Waals forces between the nanotubes. Besides, the SAED pattern of the nanotubes shows the presence of streaks and extra spots, which indicates some defects on the nanotube after the dispersion process [43]. Additionally, Fig. 3f shows the wall of the nanotubes after the dispersion process where distortions were glaringly observed. The FFT pattern of the nanotubes also indicates the increase in the interlayer spacing from 0.3461 nm of the pristine MWCNT to 0.3533 nm after the dispersion process.

Fig. 3 HRTEM micrographs of MWCNT-Ti6Al4V comprise 0.5 wt% **a** and **b**, 1.0 wt% **c** and **d**, and 1.5 wt% MWCNT **e** and **f** after SSBM process

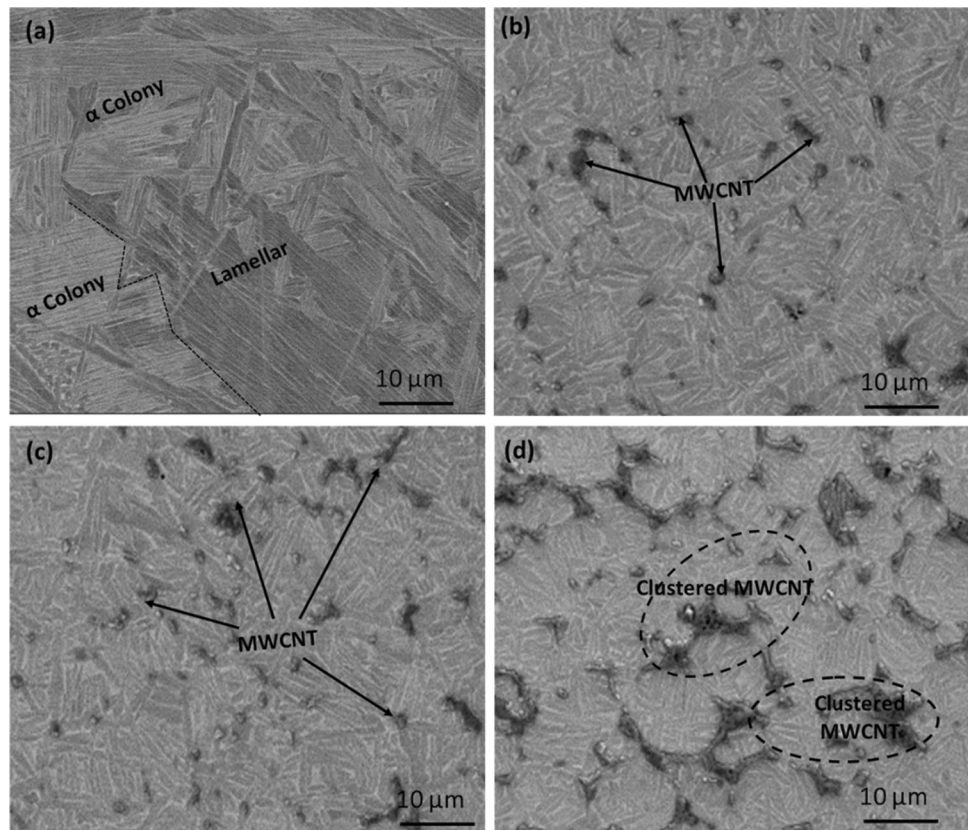


From all indications, it can be deduced that an increase in the concentration of MWCNT in the composite grades decreases their tendency for uniform dispersion and further expose the nanotubes to more structural strain during the dispersion process.

3.1.2 Microstructural Evolution of Fabricated Materials

Immediately after the dispersion process, the starting Ti6Al4V and mixed powders were consolidated using the SPS process. Figure 4a–d shows the SEM micrographs of

Fig. 4 SEM micrographs of the fabricated Ti6Al4V **a** and MWCN-Ti6Al4V nanocomposites comprising of 0.5 wt% **b**, 1.0 wt% **c**, and 1.5 wt% **d** MWCNT



the fabricated Ti6Al4V and MWCNT-Ti6Al4V nanocomposites comprising of varying concentration of the nanotubes. Figure 4a represents the SEM micrograph of the fabricated Ti6Al4V alloy, which depicts a network of alpha (α) lamellar. The microstructural features observed on the SEM micrograph of the fabricated Ti6Al4V may be attributed to sintering above the allotropic transformation temperature of Ti6Al4V and the slow cooling process in the sintering chamber. Meanwhile, sintering of Ti6Al4V above the (α/β) transformation temperature will result in grain growth irrespective of the heating rate and cooling conditions [20].

The SEM micrograph of the sintered MWCNT-Ti6Al4V nanocomposites comprising of 0.5 wt% MWCNT is shown in Fig. 4b. From the SEM micrograph, it was observed that MWCNT were dispersed across the Ti6Al4V phases. Similarly, the SEM micrograph in Fig. 4c shows the even dispersion of 1.0 wt% MWCNT across the Ti6Al4V matrix. However, a more clustered MWCNT was observed in the SEM micrograph of the nanocomposite comprising of 1.5 wt% MWCNT. These microstructural evolutions are in conformity with the SEM and TEM results of the admixed powders discussed earlier.

Subsequently, the fabricated Ti6Al4V and the corresponding nanocomposites were characterized using LM and the results are shown in Fig. 5. Figure 5a is the LM of the fabricated Ti6Al4V alloy which depicts colonies of alpha

phase lamellar. This microstructural feature, which corresponds to the SEM micrograph discussed earlier, may be ascribed to the sintering above the (α/β) transus temperature and the slow cooling process that trapped the α lamellar phases within the alloy.

Additionally, the LM micrograph of the fabricated Ti6Al4V nanocomposites comprising of 0.5 wt% MWCNT is shown in Fig. 5b where MWCNT (dark spots) were dispersed across the Ti6Al4V phases. Similarly, this microstructural feature was observed in Fig. 5c and d where the MWCNT were spread across the Ti6Al4V phases. However, more clustered MWCNT were seen in LM micrographs in Fig. 5d, which revealed the agglomeration of nanotubes at higher concentration. These results are in conformity with the SEM micrographs discussed earlier where the dispersion features decreased with an increase in concentration of MWCNT in the nanocomposites.

3.1.3 Fracture Morphology of the Fabricated Materials

In order to further ascertain the microstructural evolution and behaviour of the fabricated Ti6Al4V and the MWCNT-Ti6Al4V nanocomposites, the fractured surface of the materials was characterized under SEM and the results are shown in Fig. 6. The morphology of the fabricated alloy as shown in Fig. 6a, which depict large dimples, revealed that the alloy

Fig. 5 LM micrographs of the fabricated Ti6Al4V **a** and MWCN-Ti6Al4V nanocomposites comprising of 0.5 wt% **b**, 1.0 wt% **c**, and 1.5 wt% **d** MWCNT

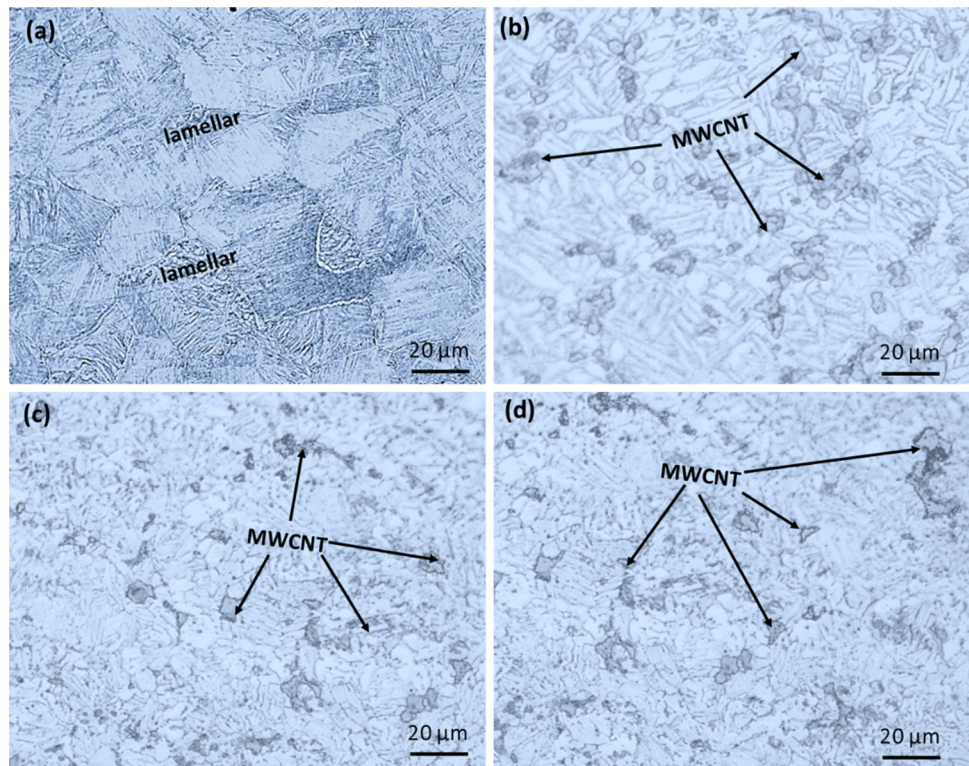
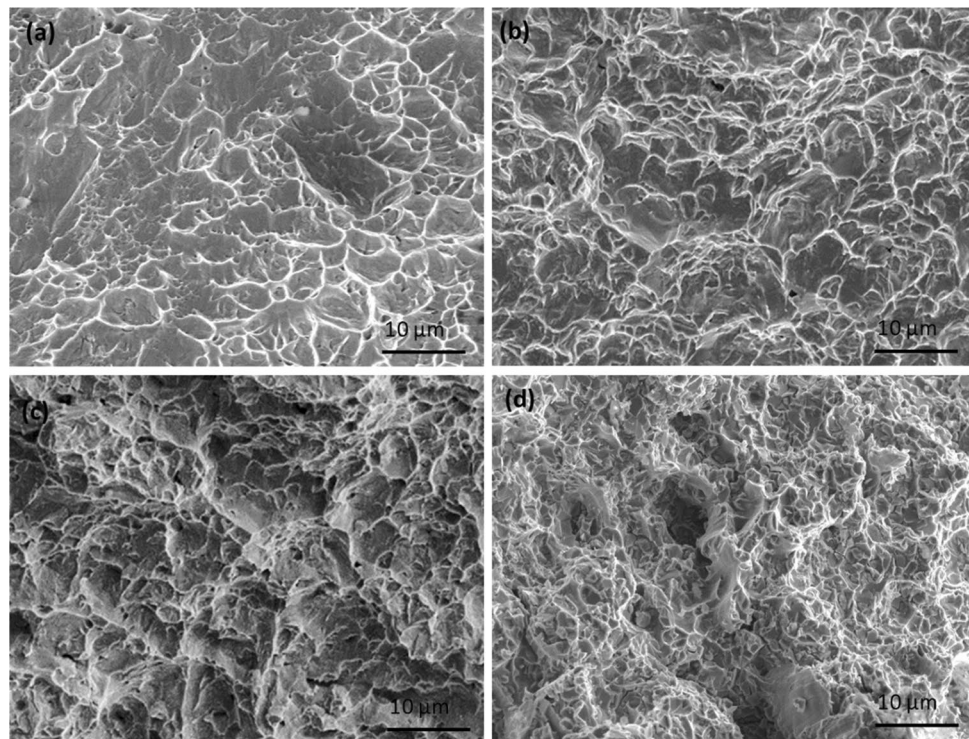


Fig. 6 Fractured Morphology of the fabricated Ti6Al4V **a** and MWCN-Ti6Al4V nanocomposites comprising of 0.5 wt% **b**, 1.0 wt% **c**, and 1.5 wt% **d** MWCNT



undergoes ductile failure mode. Similarly, the nanocomposite grade comprising of 0.5 wt% MWCNT shown in Fig. 6b depicts a dimple fracture morphology with more refined dimples and tiny voids.

Furthermore, with an increase in concentration of MWCNT to 1.0 and 1.5 wt%, distinct fracture modes were observed. The dimple fracture morphology became more refined with a mixture of both dimple-like and cleavage-like

failure. The fracture morphologies also indicated that there were reduction in the ductility of the nanocomposite with an increase in MWCNT content. However, this fracture mode suggest an improvement in the hardness and strength of the nanocomposites during loading condition. It was observed that the presence of micropores in the fabricated nanocomposites increased with the addition of MWCNT, which may result in the reduction in the density of the material. From all indications, it can be deduced that the incorporation and increase in MWCNT results in the microstructural changes of the fracture morphology of Ti6Al4V nanocomposites.

3.2 X-Ray Diffraction Analysis

The phase evolution and analysis of the starting powders, mixed powders, fabricated Ti6Al4V and the MWCN-Ti6Al4V nanocomposites were characterized using X-Ray diffraction (XRD) techniques. The XRD pattern of the starting and mixed powders is shown in Fig. 7. Figure 7a shows the XRD pattern of the starting MWCNT where the two prominent graphitic peaks were glaringly observed at $2\theta = 25.6^\circ$ and 43.3° , which coincides with the respective planes of (002) and (100).

Moreover, the XRD pattern of the starting Ti6Al4V powders shown in Fig. 7 (b) revealed only the α phases of the titanium alloy with conforming peaks at $2\theta = 35.48^\circ$, 38.68° , 40.52° , 53.43° , 63.85° , 81.10° , 86.92° , 82.84° and 88.42° . The peaks at these diffracted angles corresponds to the respective planes of (100), (002), (101), (102), (110), (103), (112), (004) and (202). The XRD patterns of the mixed powders comprising of 0.5–1.5 wt% MWCNT are shown in Fig. 7c–e.

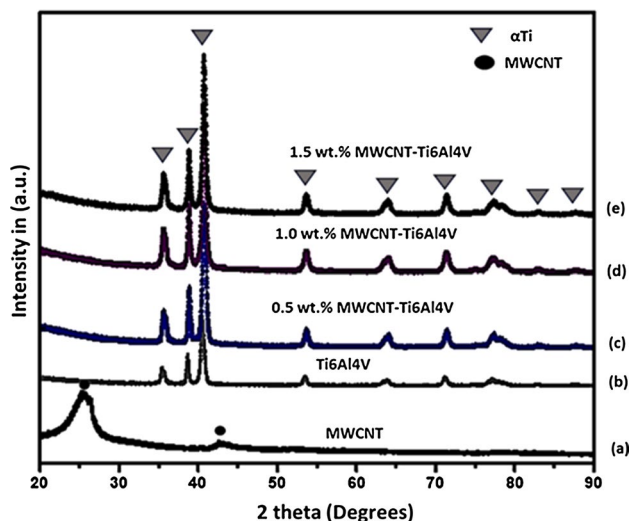


Fig. 7 XRD patterns of starting powders **a** MWCNT, **b** starting Ti6Al4V, and mixed nanocomposite powders comprising of **c** 0.5 wt% MWCNT **d** 1.0 wt% MWCNT, and **e** 1.5 wt% MWCNT

From the XRD pattern in Fig. 7c, which shows the phase evolution of the mixed powders comprising of 0.5 wt% MWCNT, α phases of the titanium alloy were more pronounced without any trace of the presence of MWCNT. Although, from the XRD patterns of the mixed powder comprising of 1.0 and 1.5 wt% MWCNT, there were more increase in the peaks of the alpha titanium phases without any trace of MWCNT. The presence of the increase in the alpha titanium peaks may be ascribed to the mechanical stresses induced on the powders during the dispersion process. Besides, the absence of MWCNT in the XRD pattern of the mixed powders may be ascribed to the low concentration of the nanotubes when compared with the matrix material. Also, it can be attributed to the difference in the coefficient of mass absorption of titanium and carbon for the Cu $K\alpha$ radiations [44]. The XRD patterns of the mixed powders also revealed that no TiC phases were formed despite the structural strain induced on the MWCNT during the dispersion process. Nonetheless, the structural strain only resulted in the increase in the alpha titanium peaks on the admixed powders during after milling.

Furthermore, the phase evolution of the fabricated alloy and nanocomposites after SPS is illustrated by the XRD pattern in Fig. 8. Apart from the XRD pattern in Fig. 8a, which shows the phase evolution of the fabricated Ti6Al4V where only the alpha titanium phases were observed, the XRD patterns of all the fabricated nanocomposites depict other phases. The MWCNT, α , β and TiC phases were glaringly observed on the XRD pattern of the fabricated nanocomposites. Meanwhile, more phase evolutions were observed on the XRD patterns of the fabricated nanocomposites comprising of 1.0 and 1.5 wt% MWCNT. Nevertheless, the alpha

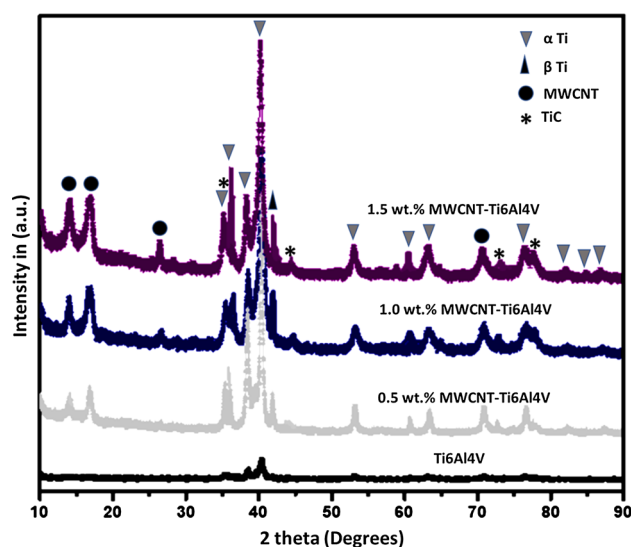


Fig. 8 XRD patterns of the fabricated Ti6Al4V and Ti6Al4V nanocomposites comprising of MWCNT (0.5–1.5 wt%)

titanium peaks was found to increase with an increase in concentration of the MWCNT. This indicates that the presence and addition of MWCNT favours the stabilization of the alpha titanium phases owing to the fact that carbon is an alpha phase stabilizer in Ti6Al4V alloy.

The XRD pattern of the fabricated nanocomposites further revealed that sintering of the nanocomposite powders at 1000 °C activated a chemical reaction between the carbon and the titanium [45]. This resulted in the formation of carbide phases, MWCNT and the beta titanium phases. Also, this is an indication that sintering at higher temperature above the alpha–beta transus temperature promote some structural and phase evolution of the nanocomposites. Furthermore, the formation of TiC (harder phase) phases after the sintering process will help to augment the strength, hardness and the anti-wear behaviour of the nanocomposites during service conditions.

3.3 Raman Spectroscopic Analysis

The structural evolution of the as-received MWCNT, mixed nanocomposites powders and the fabricated nanocomposites were ascertained by Raman spectroscopy. Figure 9a–e presents the Raman result of the starting and mixed powders comprising of varying concentration of MWCNT dispersed in Ti6Al4V matrix.

The Raman spectrum in Fig. 9a depicts the Raman result of the Ti6Al4V powder and it was observed that there were no pronounced peaks in the result. This agrees with previous studies where titanium-based matrices does not display any prominent vibration peaks during Raman analysis [26, 46, 47]. Besides, Raman analysis is usually employed to confirm the structural changes in carbon nanomaterials (graphite,

graphene, graphene nanoplatelets, graphene nanoribbon, and carbon nanotubes) during their dispersion in matrix materials. It is often used to identify the D and G bands, which helps to explain the structural integrity of the carbonaceous material during materials processing for composite production. The D band is usually associated with the non-sp² defects in the C–C bond of carbon nanomaterials while the G band is linked to the stretching mode of the plane C–C network. The G band is also used to confirm the crystalline nature, degree of graphitization and orderliness of the C–C network in carbon nanomaterials [47, 48].

In previous studies, the D and G band has been employed to ascertain the extent of defects on the walls of the nanotubes during dispersion in metal matrices and consolidation process [49, 50]. This is generally achieved by investigating the intensity ratio of the D and G band, the broadening, decrease and shift in the D and G band. The shift in the G band also induce structural defects, which is usually in the form of open edges and vacancies, on the nanotubes during their incorporation in matrix materials [51].

Furthermore, the Raman spectrum in Fig. 9b shows the Raman result of the starting MWCNT before the dispersion process. From the Raman result, it was observed that the D and G band were situated at 1340 cm⁻¹ and 1580 cm⁻¹ respectively. From Fig. 9b, the intensity ratio (I_D/I_G) of the starting MWCNT was calculated to be 0.800. However, when the MWCNT was dispersed in the Ti6Al4V powder, visible changes in the Raman spectra were observed in Fig. 9c–e. From the Raman spectrum in Fig. 9c which presents the Raman result of the mixed powder comprising of 0.5 wt% MWCNT, it was observed that the D and G band shifted to 1400 cm⁻¹ and 1630 cm⁻¹ respectively. Similarly, an incredible increase in the intensity ratio (I_D/I_G) of the D and G band from 0.800 in the starting MWCNT to 0.857 was noticed. The incredible change in intensity ratio translates to 7.13% increase of I_D/I_G ratio of the mixed powder comprising of 0.5 wt% MWCNT. The Raman shift and increase in the intensity ratio of the D and G band recorded maybe ascribed to the strain induced on the nanotubes during the dispersion process.

Subsequently, the Raman result of the mixed powder comprising of 1.0 wt% MWCNT is shown in Fig. 9d. From the Raman spectrum in Fig. 9d, the D and G band were situated at an higher wavenumber of 1402 cm⁻¹ and 1632 cm⁻¹ respectively. The intensity ratio of the D and G band experienced similar increase from 0.800 in the starting MWCNT to 0.905, which can be calculated as 13.13% increased. Similarly, the Raman result of the mixed powder comprising of 1.5 wt% MWCNT shown in Fig. 9e experienced a slight Raman shift. The D and G band experienced incredible

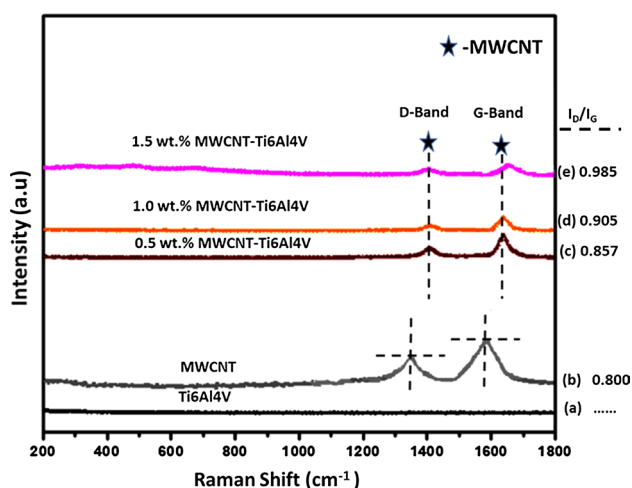


Fig. 9 Raman spectra of starting powders **a** Ti6Al4V, **b** starting MWCNT, and mixed nanocomposite powders comprising of **c** 0.5 wt% MWCNT **d** 1.0 wt% MWCNT, and **e** 1.5 wt% MWCNT

shifts to higher wavenumbers of 1403 cm^{-1} and 1648 cm^{-1} with a corresponding increase in I_D/I_G ratio to 0.985, which amounts to 23.13% increased. A detailed analysis of the Raman shift indicates that there was a higher shift in the G band when the concentration of the MWCNT was increased to 1.5 wt%. This implies that the MWCNT in the nanocomposite grade was exposed to considerable deformation during the dispersion process. Besides, a similar change in the SAED pattern of this nanocomposite grade was observed earlier. However, the considerable deformation on the walls of the nanotubes does not translate to the formation of carbide phases during the dispersion process.

Furthermore, the Raman results of the starting MWCNT, fabricated alloy and nanocomposites are presented in Fig. 10a–e. A thorough examination of the Raman spectra of the fabricated nanocomposites showed the evolution of new vibration peaks at 265 cm^{-1} , 416 cm^{-1} and 602 cm^{-1} wavenumbers. Previous studies have emphasised that these peaks are associated with the TiC phases formed on the MWCNT during the consolidation process [52–54]. The Raman spectrum in Fig. 10c shows the Raman result of the fabricated nanocomposite comprising of 0.5 wt% MWCNT. It was observed from the Raman result that the D and G bands were situated at higher wavenumber of 1406 cm^{-1} and 1635 cm^{-1} respectively. Correspondingly, the I_D/I_G increased from 0.800 in the starting MWCNT to 0.927, which amounts to an increase of 15.88%. Similarly, the Raman result of the fabricated nanocomposite comprising of 1.0 wt% MWCNT is shown in Fig. 10d. From the Raman result, it was observed that the D and G bands shifted to a higher wavenumber of 1408 cm^{-1} and 1637 cm^{-1} with an I_D/I_G ratio of 0.979, which represent an increase of 22.38%.

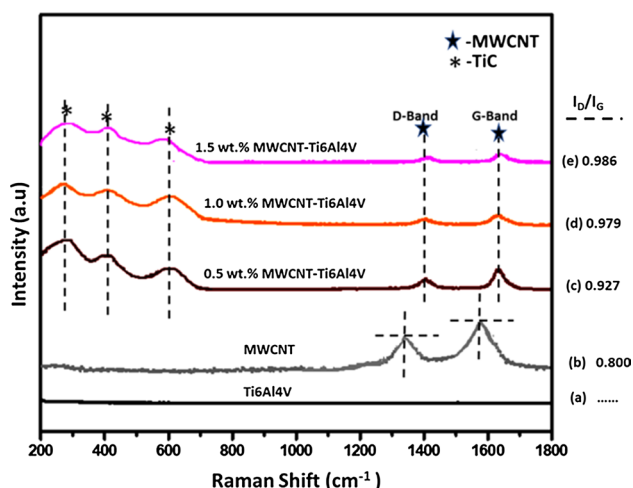


Fig. 10 Raman spectra of starting MWCNT **a** consolidated Ti6Al4V **b** and nanocomposites comprising of **c** 0.5 wt% MWCNT **d** 1.0 wt% MWCNT, and **e** 1.5 wt% MWCNT

Likewise, similar trends on the shift of the D and G band and increase in I_D/I_G ratio were observed from the Raman spectrum in Fig. 10e. The Raman spectrum in Fig. 10e shows the Raman result of the fabricated nanocomposites comprising of 1.5 wt% MWCNT and it was observed that the D and G band shifted to a higher wavenumber of 1412 cm^{-1} and 1658 cm^{-1} respectively. The I_D/I_G ratio also increased to 0.986 from 0.800 in the starting MWCNT, which amounts to an increase of 23.25%. The Raman shift of the D and G band with the corresponding increase in the intensity ratio after the fabrication process maybe ascribed to the thermomechanical stresses during dispersion and the sintering, which was induced on the walls of the nanotubes. The stresses induced on the MWCNT during consolidation resulted in the formation of carbide phases observed from the Raman spectra. Consequently, this can assist in improving the mechanical properties of the nanocomposites during service conditions.

3.4 Density Measurement of the Fabricated Materials

To understand the integrity of the fabricated alloy and nanocomposites, the densification of the nanocomposites were investigated and the results are shown in Fig. 11. From Fig. 11, it was seen that the density of the materials was in the range of 98.7 to 99.7%, which declined with an increase in concentration of the MWCNT. Furthermore, the pure alloy displayed the highest density value of 99.66%, which indicates that there were less porosity in the fabricated alloy, which was confirmed from the SEM morphology and fractography presented earlier. Conversely, with the introduction and increase in the concentration of MWCNT in the Ti6Al4V matrix, the density declined intermittently. The fabricated nanocomposite with 0.5 wt% MWCNT displayed a density value of 99.4% followed by the nanocomposite with 1.0 wt% MWCNT, which has a relative density value

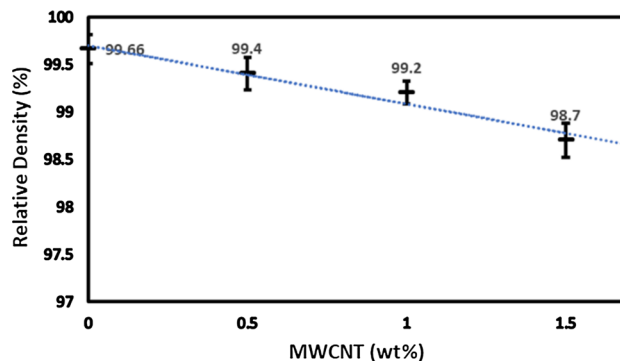


Fig. 11 Density of the consolidated Ti6Al4V and Ti6Al4V based nanocomposites

of 99.2%. The nanocomposite with 1.5 wt% MWCNT displayed the least relative density value of 98.7%.

From the results of the relative density of the fabricated alloy and nanocomposites, it can be deduced that the addition of MWCNT into the Ti6Al4V matrix introduced some micropores that eventually translate to the reduction of the density of the nanocomposites. This indicates that an increase in the concentration of MWCNT resulted in a decrease in the relative density of the fabricated nanocomposites. Also, the presence of micropores were observed in the fractography of the fabricated nanocomposites. These results are in accordance with results obtained from previous studies where MWCNT was incorporated in metal matrices to improve their properties [55, 56].

3.5 Mechanical Properties

3.5.1 Micro and Nanohardness Values of the Fabricated Materials

The mechanical properties of the fabricated alloy and nanocomposites were investigated using Vickers microhardness tester and nanoindentation technique. The results obtained from the investigations were used to derive an equation relating the microhardness and nanohardness of the fabricated

materials. Furthermore, the microhardness nanohardness results and the derived relationship are presented in Fig. 12.

The Vickers microhardness values of the fabricated alloy and nanocomposites are presented in Fig. 12a. From the microhardness results, it was observed that the microhardness values improved with the incorporation and increase in concentration of the MWCNT in the nanocomposites. Meanwhile, the nanocomposite grade comprising of 1.5 wt% MWCNT displayed the highest microhardness value of 569.8 HV followed by the nanocomposite grade comprising of 1.0 wt% which has a microhardness value of 485.3 HV. This was accompanied by the nanocomposite grade comprising of 0.5 wt% MWCNT, which displayed a microhardness value of 463.1 HV. Conversely, the fabricated Ti6Al4V showed the least microhardness value of 388 HV. The improvement in the microhardness value can be ascribed to the incorporation and increase in concentration of MWCNT, which strengthened the Ti6Al4V matrix via the dispersion strengthening mechanism and the pinning effect [57]. Besides, the presence of the TiC phases formed in the nanocomposites assisted in augmenting the hardness of the fabricated nanocomposites.

Similarly, the results of the nanohardness of the fabricated alloy and nanocomposites are presented in Fig. 12b. The nanohardness results follow similar trends as the

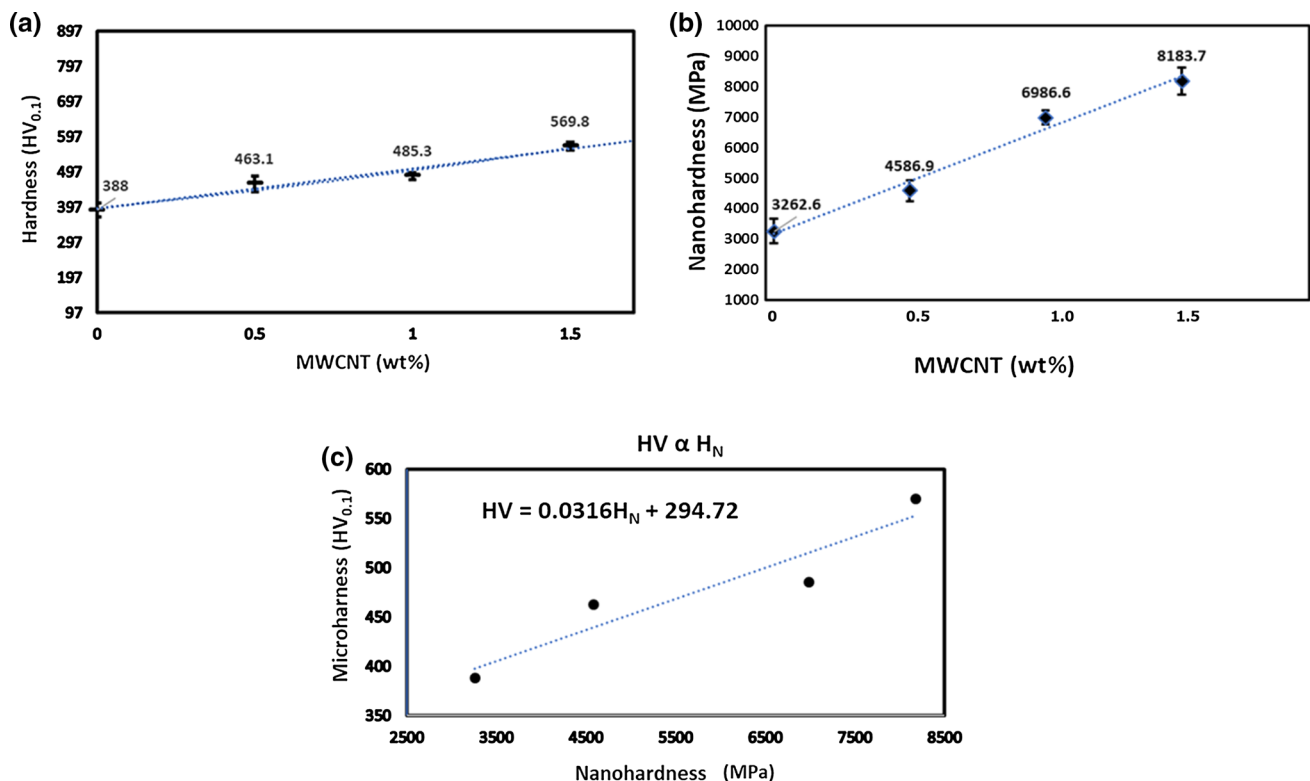


Fig. 12 Microhardness (a) and nanohardness results (b), and the relationships between microhardness and nanohardness results (c) of the fabricated Ti6Al4V and its nanocomposites

microhardness values discussed earlier. The nanohardness value improved with the incorporation and increase in the concentration of MWCNT. This was evident as the nanocomposite grade comprising of 0.5 wt% MWCNT has a nanohardness of 4586.9 MPa while the 1.0 wt% MWCNT-reinforced nanocomposite grade has a nanohardness of 6986.6 MPa. The best nanohardness of 8183.7 MPa was obtained for the nanocomposite grade reinforced with 1.5 wt% MWCNT. Nevertheless, the fabricated Ti6Al4V alloy has the least nanohardness value of 3262.6 MPa.

From all indications, the microhardness and nanohardness of the fabricated nanocomposites increased with the incorporation of MWCNT into the Ti6Al4V matrix. This increased could be ascribed to the presence of the insitu TiC phases formed during the consolidation of the nanocomposites. In addition, the presence of MWCNT in the Ti6Al4V matrix created a higher dislocation density during consolidation resulting from the difference in the coefficient of thermal expansion between the nanotubes and the Ti6Al4V matrix. The higher dislocation density formed assisted in obstructing the dislocation motion resulting in the improvement of the mechanical properties [46, 58]. Furthermore, the improvements could be attributed to the dispersion strengthening, work hardening, Orowan looping and grain boundary hardening of the MWCNT, which inhibit the dislocation motion during indentation of the nanocomposites. The improvement in hardness can as well be traced to the densification achieved, the transfer of load from the matrix phase to the MWCNT and the interfacial bonding between the composite components. The work hardening effect (WHE) of the MWCNT [59] is expressed in Eq. (3).

$$H_{WHE} = K_w \rho_{dis}^{1/2} = \alpha G b \rho_{dis}^{1/2} \quad (3)$$

where K_w represent the strength index, ρ_{dis} is the dislocation density of the grain interior, α is a constant while G is the shear modulus of the MWCNT, and b signifies the Burger vector. Similarly, the grain boundary hardening can be expressed as the Hall–Petch relationship [59], which is expressed in Eq. (4).

$$H_{GPH} = K_H d^{-1/2} \quad (4)$$

where K_H is equivalent to $0.14 \text{ MPam}^{1/2}$ and d represents the grain size. Besides, the derived relationship between the microhardness and nanohardness is shown in Eq. (5).

$$H_V = 0.0316 H_N + 294.72 \quad (5)$$

3.5.2 Load–Displacement Plots of the Fabricated Materials

The mechanical behaviour of the fabricated alloy and nanocomposites was further investigated by nanoindentation

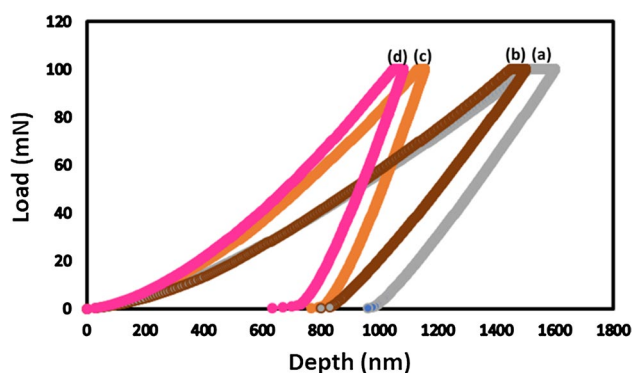


Fig. 13 Load–displacement curves of the fabricated Ti6Al4V a, and Ti6Al4V nanocomposites comprising of 0.5 wt% MWCNT b, 1.0 wt% MWCNT c, and 1.5 wt% MWCNT d

technique. The load–displacement plot during nanoindentation is presented in Fig. 13a–d. From the indentation curve in Fig. 13a, which shows the loading and unloading curve of the fabricated alloy, it was observed that the alloy undergoes considerable plastic deformation during the indentation that was reflected in the indentation depth of 976.5 nm.

The nanocomposites grade comprising of 0.5 wt% MWCNT displayed the least resistance to plastic deformation during the nanoindentation. This was followed by the nanocomposite grade comprising of 1.0 wt% MWCNT with an indentation depth of 730 nm, which has a higher resistance to plastic deformation. However, the nanocomposite grade comprising of 1.5 wt% MWCNT was found to display the highest resistance to plastic deformation among the fabricated nanocomposites with an indentation depth of 634 nm. These load–displacement results imply that the incorporation and increase in the concentration of MWCNT improved its resistance to plastic deformation during nanoindentation. Therefore, the presence of MWCNT in the nanocomposite grades helps to strengthen and stiffen the Ti6Al4V matrix.

3.5.3 Elastic Modulus of the Fabricated Materials

To further ascertain the mechanical behaviour of the fabricated alloy and nanocomposites, the elastic modulus of the materials was investigated using nanoindentation. The elastic modulus results of the fabricated materials are presented in Fig. 14. From this Figure, it was observed that the elastic modulus of the materials improved with the incorporation and increase in the concentration of MWCNT in the nanocomposites.

Meanwhile, the fabricated Ti6Al4V displayed the least elastic modulus value of 24.51 GPa and this was followed by the nanocomposite grade comprising of 0.5 wt% MWCNT with an elastic modulus value of 28.02 GPa. Besides, the nanocomposite grade comprising of 1.5 wt% MWCNT exhibit the highest elastic modulus result with

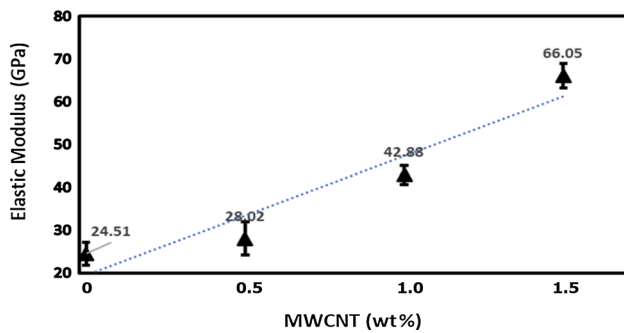


Fig. 14 Elastic Modulus of the fabricated Ti6Al4V and nanocomposites

a value of 66.05 GPa, which further explained that this nanocomposite grade demonstrated the highest elastic resistance to linear compression from the indenter. In a nutshell, the incorporation of MWCNT into Ti6Al4V improved the elastic modulus of the metal matrix. This improvement can also be ascribed to the presence of the secondary carbide phases formed during the consolidation of the nanocomposites.

4 Conclusion

In this study, the influence of MWCNT contents on the microstructural evolution and mechanical properties of spark plasma sintered Ti6Al4V based nanocomposites was investigated. Prior to the consolidation of the nanocomposites, MWCNT were dispersed in the Ti6Al4V matrix by shift speed ball milling technique and then consolidated via the spark plasma sintering technique. Various characterization techniques and mechanical tests were carried out to ascertain the influence of MWCNT contents on the microstructural evolution and properties of the nanocomposites. The following conclusions were drawn from the investigations;

- 1 Microstructural evolutions from the SEM, TEM and light microscopy confirmed that the MWCNT were fully dispersed in the Ti6Al4V matrix.
- 2 Increase in the concentration of MWCNT adversely influence their dispersibility in Ti6Al4V matrix after SSBM and SPS.
- 3 The incorporation and increase in the concentration of MWCNT in the Ti6Al4V matrix introduced some micropores in the nanocomposites.
- 4 Mechanical properties such as microhardness, nanohardness and elastic modulus were tremendously improved by the incorporation and increase in the concentration of MWCNT in the Ti6Al4V matrix.

Acknowledgement This research was fully funded by the National Research Foundation of South Africa and the Global Excellence and Stature (GES) of the University of Johannesburg, South Africa.

References

1. K.S. Munir, Y. Zheng, D. Zhang, J. Lin, Y. Li, C. Wen, Microstructure and mechanical properties of carbon nanotubes reinforced titanium matrix composites fabricated via spark plasma sintering. *Mater. Sci. Eng. A.* **688**, 505–523 (2017). <https://doi.org/10.1016/j.msea.2017.02.019>
2. R.S. Ruoff, D. Qian, W.K. Liu, Mechanical properties of carbon nanotubes: theoretical predictions and experimental measurements. *Comptes Rendus Phys.* **4**, 993–1008 (2003)
3. E.W. Wong, P.E. Sheehan, C.M. Lieber, Nanobeam mechanics: elasticity, strength, and toughness of nanorods and nanotubes. *Science* **80**(277), 1971–1975 (1997)
4. S. Berber, Y.-K. Kwon, D. Tománek, Unusually high thermal conductivity of carbon nanotubes. *Phys. Rev. Lett.* **84**, 4613 (2000)
5. T.W. Ebbesen, H.J. Lezec, H. Hiura, J.W. Bennett, H.F. Ghaemi, T. Thio, Electrical conductivity of individual carbon nanotubes. *Nature* **382**, 54 (1996)
6. K.S. Munir, Y. Li, D. Liang, M. Qian, W. Xu, C. Wen, Effect of dispersion method on the deterioration, interfacial interactions and re-agglomeration of carbon nanotubes in titanium metal matrix composites. *Mater. Des.* **88**, 138–148 (2015). <https://doi.org/10.1016/j.matdes.2015.08.112>
7. B. Chen, J. Shen, X. Ye, L. Jia, S. Li, J. Umeda, M. Takahashi, K. Kondoh, Length effect of carbon nanotubes on the strengthening mechanisms in metal matrix composites. *Acta Mater.* **140**, 317–325 (2017). <https://doi.org/10.1016/j.actamat.2017.08.048>
8. A.M. Okoro, R. Machaka, S.S. Lephuthing, M.A. Awotunde, S.R. Oke, O.E. Falodun, P.A. Olubambi, Dispersion characteristics, interfacial bonding and nanostructural evolution of MWCNT in Ti6Al4V powders prepared by shift speed ball milling technique. *J. Alloys Compd.* **785**, 356–366 (2019)
9. J.-W. An, D.-H. You, D.-S. Lim, Tribological properties of hot-pressed alumina–CNT composites. *Wear* **255**, 677–681 (2003)
10. P. Guo, X. Chen, X. Gao, H. Song, H. Shen, Fabrication and mechanical properties of well-dispersed multiwalled carbon nanotubes/epoxy composites. *Compos. Sci. Technol.* **67**, 3331–3337 (2007)
11. A.M.K. Esawi, K. Morsi, A. Sayed, M. Taher, S. Lanka, Effect of carbon nanotube (CNT) content on the mechanical properties of CNT-reinforced aluminium composites. *Compos. Sci. Technol.* **70**, 2237–2241 (2010). <https://doi.org/10.1016/j.compscitech.2010.05.004>
12. N. Selvakumar, K. Gangatharan, Electrical resistivity, tribological behaviour of multiwalled carbon nanotubes and nanoboron carbide particles reinforced copper hybrid composites for pantograph application. *Adv. Mater. Sci. Eng.* **2016**, 1–18 (2016)
13. K.S. Munir, Y. Zheng, D. Zhang, J. Lin, Y. Li, C. Wen, Improving the strengthening efficiency of carbon nanotubes in titanium metal matrix composites. *Mater. Sci. Eng. A.* **696**, 10–25 (2017). <https://doi.org/10.1016/j.msea.2017.04.026>
14. A.M. Okoro, S.S. Lephuthing, S.R. Oke, O.E. Falodun, M.A. Awotunde, P.A. Olubambi, A Review of Spark Plasma Sintering of Carbon Nanotubes Reinforced Titanium-Based Nanocomposites: fabrication, densification, and mechanical properties. *JOM.* (2018). <https://doi.org/10.1007/s11837-018-3277-2>
15. O.E. Falodun, B.A. Obadele, S.R. Oke, A.M. Okoro, P.A. Olubambi, Titanium-based matrix composites reinforced with particulate, microstructure, and mechanical properties using spark

- plasma sintering technique: a review. *Int. J. Adv. Manuf. Technol.* 1–13 (2019)
16. S. Li, B. Sun, H. Imai, T. Mimoto, K. Kondoh, Powder metallurgy titanium metal matrix composites reinforced with carbon nanotubes and graphite. *Compos. Part A Appl. Sci. Manuf.* **48**, 57–66 (2013). <https://doi.org/10.1016/j.compositesa.2012.12.005>
 17. A.M. Okoro, M. Awotunde, O.A. Ajiteru, S.S. Lephuthing, P.A. Olubambi, R. Machaka, Effects of carbon nanotubes on the mechanical properties of spark plasma sintered titanium matrix composites—a review, in 2018 IEEE 9th International Conference of Mechanical Intelligent Manufacturing Technologies ICMIMT 2018. (2018). <https://doi.org/10.1109/ICMIMT.2018.8340420>
 18. J.D. Majumdar, I. Manna, Laser surface engineering of titanium and its alloys for improved wear, corrosion and high-temperature oxidation resistance, in: *Laser Surf. Eng.*, Elsevier, pp. 483–521 (2015)
 19. A.K.M.N. Amin, Titanium alloys-towards achieving enhanced properties for diversified applications. (2012)
 20. G.F. Batalha, M. Motyka, K. Kubiak, J. Sieniawski, W. Ziaja, D.J. Dos Santos, D.J. Carastan, L.B. Tavares, F. Buiocchi, M.A.B. Andrade, others, Editorial Board Contributors to Volume 2 Preface xv, *Compr. Mater. Process.* (2014)
 21. C. Leyens, M. Peters, *Titanium and titanium alloys: fundamentals and applications* (John Wiley & Sons, New Jersey, 2003)
 22. O.E. Falodun, B.A. Obadele, S.R. Oke, O.O. Ige, P.A. Olubambi, Effect of TiN and TiCN additions on spark plasma sintered Ti–6Al–4V. *Part. Sci. Technol.* 1–10 (2018)
 23. B. Zhao, W.F. Ding, J.B. Dai, X.X. Xi, J.H. Xu, A comparison between conventional speed grinding and super-high speed grinding of (TiC p+ TiB w)/Ti–6Al–4V composites using vitrified CBN wheel. *Int. J. Adv. Manuf. Technol.* **72**, 69–75 (2014)
 24. K. Kondoh, T. Threrujirapapong, H. Imai, J. Umeda, B. Fugetsu, Characteristics of powder metallurgy pure titanium matrix composite reinforced with multi-wall carbon nanotubes. *Compos. Sci. Technol.* **69**, 1077–1081 (2009). <https://doi.org/10.1016/j.compscitech.2009.01.026>
 25. X. Sun, Y. Han, S. Cao, P. Qiu, W. Lu, Rapid in-situ reaction synthesis of novel TiC and carbon nanotubes reinforced titanium matrix composites. *J. Mater. Sci. Technol.* **33**, 1165–1171 (2017)
 26. K.S. Munir, M. Qian, Y. Li, D.T. Oldfield, P. Kingshott, D.M. Zhu, C. Wen, Quantitative analyses of MWCNT-Ti powder mixtures using Raman spectroscopy: the influence of milling parameters on nanostructural evolution. *Adv. Eng. Mater.* **17**, 1660–1669 (2015)
 27. E. Thostenson, Advances in the science and technology of carbon nanotubes and their composites: a review. *Compos. Sci. Technol.* **61**, 1899–1912 (2001). [https://doi.org/10.1016/S0266-3538\(01\)00094-X](https://doi.org/10.1016/S0266-3538(01)00094-X)
 28. L. Ci, Z. Ryu, N.Y. Jin-Phillipp, M. Rühle, Investigation of the interfacial reaction between multi-walled carbon nanotubes and aluminum. *Acta Mater.* **54**, 5367–5375 (2006)
 29. M.R. Piggott, The interface in carbon fibre composites. *Carbon N. Y.* **27**, 657–662 (1989)
 30. F.C. Wang, Z.H. Zhang, Y.J. Sun, Y. Liu, Z.Y. Hu, H. Wang, A.V. Korznikov, E. Korznikova, Z.F. Liu, S. Osamu, Rapid and low temperature spark plasma sintering synthesis of novel carbon nanotube reinforced titanium matrix composites. *Carbon N. Y.* **95**, 396–407 (2015). <https://doi.org/10.1016/j.carbon.2015.08.061>
 31. A.O. Adegbenjo, P.A. Olubambi, J.H. Potgieter, E. Nsiha-Baafi, M.B. Shongwe, Interfacial reaction during high energy ball milling dispersion of carbon nanotubes into Ti6Al4V. *J. Mater. Eng. Perform.* **26**, 6047–6056 (2017). <https://doi.org/10.1007/s11665-017-3041-8>
 32. F. Mokdad, D.L. Chen, Z.Y. Liu, B.L. Xiao, D.R. Ni, Z.Y. Ma, Deformation and strengthening mechanisms of a carbon nanotube reinforced aluminum composite. *Carbon N. Y.* **104**, 64–77 (2016). <https://doi.org/10.1016/j.carbon.2016.03.038>
 33. R. Spectrometers, Standard guide for Raman shift standards for spectrometer calibration **1**(96), 1–11 (2014). 10.1520/E1840-96R07.2
 34. A.S. for Testing, M.C.B. on Metal Powders, M.P. Products, Standard Test Methods for Density of Compacted or Sintered Powder Metallurgy (PM) Products Using Archimedes' Principle, ASTM International, (2009)
 35. G.M. Pharr, W.C. Oliver, F.R. Brotzen, On the generality of the relationship among contact stiffness, contact area, and elastic modulus during indentation. *J. Mater. Res.* **7**, 613–617 (1992)
 36. B.B. Medeiros, M.M. Medeiros, J. Fornell, J. Sort, M.D. Baró, A.M.J. Junior, Nanoindentation response of Cu–Ti based metallic glasses: comparison between as-cast, relaxed and devitrified states. *J. Non. Cryst. Solids.* **425**, 103–109 (2015)
 37. P.S.R. Sreekanth, K. Acharyya, I. Talukdar, S. Kanagaraj, Studies on structural defects on 60Co irradiated multi walled carbon nanotubes. *Procedia Mater. Sci.* **6**, 1967–1975 (2014)
 38. J.H. Lehman, M. Terrones, E. Mansfield, K.E. Hurst, V. Meunier, Evaluating the characteristics of multiwall carbon nanotubes. *Carbon N. Y.* **49**, 2581–2602 (2011). <https://doi.org/10.1016/j.carbon.2011.03.028>
 39. K.S. Munir, Y. Li, M. Qian, C. Wen, Identifying and understanding the effect of milling energy on the synthesis of carbon nanotubes reinforced titanium metal matrix composites. *Carbon N. Y.* **99**, 384–397 (2016). <https://doi.org/10.1016/j.carbon.2015.12.041>
 40. K.S. Munir, C. Wen, Deterioration of the strong sp² carbon network in carbon nanotubes during the mechanical dispersion processing—a review. *Crit. Rev. Solid State Mater. Sci.* **41**, 347–366 (2016)
 41. B. Chen, J. Shen, X. Ye, H. Imai, J. Umeda, M. Takahashi, K. Kondoh, Solid-state interfacial reaction and load transfer efficiency in carbon nanotubes (CNTs)-reinforced aluminum matrix composites. *Carbon N. Y.* **114**, 198–208 (2017). <https://doi.org/10.1016/j.carbon.2016.12.013>
 42. M. Chen, G. Fan, Z. Tan, D. Xiong, Q. Guo, Y. Su, J. Zhang, Z. Li, M. Naito, Z. Di, Design of an efficient flake powder metallurgy route to fabricate CNT/6061Al composites. *Mater. Des.* **128**, 288–296 (2018). <https://doi.org/10.1016/j.matdes.2018.01.044>
 43. M.A. Asadabad, M.J. Eskandari, *Modern Electron Microscopy in Physical and Life Sciences*, Mod. Electron Microsc. Phys. Life Sci. 3–26. (2016). doi:10.5772/60494
 44. L.L. Ye, M.X. Quan, Synthesis of nanocrystalline TiC powders by mechanical alloying. *Nanostructured Mater.* **5**, 25–31 (1995)
 45. L. Xie, C. Jiang, V. Ji, Thermal relaxation of residual stresses in shot peened surface layer of (TiB+ TiC)/Ti–6Al–4V composite at elevated temperatures. *Mater. Sci. Eng. A.* **528**, 6478–6483 (2011)
 46. A.O. Adegbenjo, P.A. Olubambi, J.H. Potgieter, M.B. Shongwe, M. Ramakokovhu, Spark plasma sintering of graphitized multi-walled carbon nanotube reinforced Ti6Al4V. *Mater. Des.* **128**, 119–129 (2017). <https://doi.org/10.1016/j.matdes.2017.05.003>
 47. A.M. Okoro, R. Machaka, S.S. Lephuthing, M. Awotunde, P.A. Olubambi, Structural integrity and dispersion characteristics of carbon nanotubes in titanium-based alloy, in: *IOP Conf. Ser. Mater. Sci. Eng.*, (2018). doi:10.1088/1757-899X/430/1/012004
 48. A.C. Ferrari, Raman spectroscopy of graphene and graphite: disorder, electron-phonon coupling, doping and nonadiabatic effects. *Solid State Commun.* **143**, 47–57 (2007)
 49. T. Peng, I. Chang, Mechanical alloying of multi-walled carbon nanotubes reinforced aluminum composite powder. *Powder Technol.* **266**, 7–15 (2014). <https://doi.org/10.1016/j.powtec.2014.05.068>
 50. V. Datsyuk, M. Kalyva, K. Papagelis, J. Parthenios, D. Tasis, A. Siokou, I. Kallitsis, C. Galiotis, Chemical oxidation of multiwalled carbon nanotubes. *Carbon N. Y.* **46**, 833–840 (2008). <https://doi.org/10.1016/j.carbon.2008.02.012>

51. P. Delhaes, M. Couzi, M. Trinquedoste, J. Dentzer, H. Hamidou, C. Vix-Guterl, A comparison between Raman spectroscopy and surface characterizations of multiwall carbon nanotubes. *Carbon N. Y.* **44**, 3005–3013 (2006)
52. B.H. Lohse, A. Calka, D. Wexler, Raman spectroscopy sheds new light on TiC formation during the controlled milling of titanium and carbon. *J. Alloys Compd.* **434**, 405–409 (2007)
53. M.V. Klein, J.A. Holy, W.S. Williams, Raman scattering induced by carbon vacancies in Ti C x. *Phys. Rev. B.* **17**, 1546 (1978)
54. K.S. Munir, Y. Li, J. Lin, C. Wen, Interdependencies between graphitization of carbon nanotubes and strengthening mechanisms in titanium matrix composites. *Materialia.* (2018)
55. A. Adegbenjo, P. Olubambi, J. Potgieter, Improving the tribological properties of Ti6AL4V alloy with multi-walled carbon nanotube additions. in: *Int. Conf. Theor. Appl. Exp. Mech.*, 2018: pp. 55–61.
56. N. Saheb, Sintering behavior of CNT reinforced Al6061 and Al2124 Nanocomposites, *Adv. Mater. Sci. Eng.* 2014, (2014)
57. D. Lin, M. Saei, S. Suslov, S. Jin, G.J. Cheng, Super-strengthening and stabilizing with carbon nanotube harnessed high density nanotwins in metals by shock loading. *Sci. Rep.* **5**, 15405 (2015)
58. B. Abbasipour, B. Niroumand, S.M.M. Vaghefi, Compcasting of A356-CNT composite. *Trans. Nonferrous Met. Soc. China.* **20**, 1561–1566 (2010)
59. N. Hansen, Hall–Petch relation and boundary strengthening, 51, (2004). 801–806. doi:10.1016/j.scriptamat.2004.06.002.

Publisher's Note Springer Nature remains neutral with regard to jurisdictional claims in published maps and institutional affiliations.